Real-time laser differential confocal microscopy without sample reflectivity effects

Lirong Qiu, Dali Liu, Weiqian Zhao,* Han Cui, and Zhong Sheng

Beijing Key Laboratory for Precision Optoelectronic Measurement Instrument and Technology, School of Optoelectronics, Beijing Institute of Technology, Beijing 100081, China
zwq669@126.com

Abstract: A new real-time laser differential confocal microscopy (RLDCM) without sample reflectivity difference effects is proposed for imaging height topography of sample surface, which divides the confocal microscopy imaging light path into two confocal microscopy imaging paths before and after focus with the equal axial detector offset oriented in opposite direction. By dividing the difference of the two signals simultaneously detected from these two confocal imaging paths by the higher signal between these two signals, RLDCM separates the signal that comes from reflectivity heterogeneity from the topographic signal in real time for the first time. RLDCM significantly reduces the height topography imaging time by single-layer scanning for the sample surface with reflectivity heterogeneity, and it achieves high axial resolution and lateral resolution similar to CM by optimizing the axial detector offset. Theoretical analysis and experimental results demonstrate that RLDCM realizes the real-time surface imaging for line structures featuring Silicon Dioxide steps on a Silicon base and achieves 2-nm axial depth resolution without reducing lateral resolution.

OCIS codes: (180.1790) Confocal microscopy; (180.5810) Scanning microscopy; (120.6650) Surface measurements, figure; (100.3010) Image reconstruction techniques.

References and links

1. M. Gu, *Three-Dimensional Imaging in Confocal Microscopes* (World Scientific, 1996), chap.3.
2. T. Wilson, *Confocal microscopy* (Academic, 1990), chap.1.
3. K. Taehoon, K. Taejoong, L. Seung Woo, G. Dae-Gab, and S. Jungwoo, "Optimum conditions for high-quality 3D reconstruction in confocal scanning microscopy," Proc. SPIE **6090**, 181–187 (2006).
4. A. K. Ruprecht, T. F. Wiesendanger, and H. J. Tiziani, "Signal evaluation for high-speed confocal measurements," Appl. Opt. **41**(35), 7410–7415 (2002).
5. T. Wilson and S. J. Hewlett, "Superresolution in confocal scanning microscopy," Opt. Lett. **16**(14), 1062–1064 (1991).
6. M. Martinez-Corral, C. Ibáñez-López, G. Saavedra, and M. Caballero, "Axial gain resolution in optical sectioning fluorescence microscopy by shaded-ring filters," Opt. Express **11**(15), 1740–1745 (2003).
7. W. Zhao, L. Qiu, S. Chen, and Z. Feng, "Image Restoration Phase-Filtering Lateral Superresolution Confocal Microscopy," Chin. Phys. Lett. **23**(4), 856–859 (2006).
8. Z. Li, K. Herrmann, and F. Pohlenz, "Lateral scanning confocal microscopy for the determination of in-plane displacements of microelectromechanical systems devices," Opt. Lett. **32**(12), 1743–1745 (2007).
9. J. F. Aguilar, M. Lera, and C. J. R. Sheppard, "Imaging of spheres and surface profiling by confocal microscopy," Appl. Opt. **39**(25), 4621–4628 (2000).
10. H. Yu, T. Chen, and J. Qu, "Improving FRET efficiency measurement in confocal microscopy imaging," Chin. Opt. Lett. **8**(10), 947–949 (2010).
11. C. L. Arrasmith, D. L. Dickensheets, and A. Mahadevan-Jansen, "MEMS-based handheld confocal microscope for in-vivo skin imaging," Opt. Express **18**(4), 3805–3819 (2010).
12. M. Visscher and K. G. Struik, "Optical profilometry and its application to mechanically inaccessible surfaces Part I: Principles of focus error detection," Precis. Eng. **16**(3), 192–198 (1994).
13. C. Lee and J. Wang, "Noninterferometric differential confocal microscopywith 2-nm depth resolution," Opt. Commun. **135**(4-6), 233–237 (1997).
14. C. W. Tsai, C. H. Lee, and J. Wang, "Deconvolution of local surface response from topography in nanometer profilometry with a dual-scan method," Opt. Lett. **24**(23), 1732–1734 (1999).
15. M. Gu and C. J. R. Sheppard, "Effects of defocus and primary spherical aberration on images of a straight edge in confocal microscopy," Appl. Opt. **33**(4), 625–630 (1994).

#214706 - $15.00 USD Received 25 Jun 2014; revised 13 Aug 2014; accepted 24 Aug 2014; published 29 Aug 2014

16. W. Zhao, J. Tan, and L. Qiu, "Bipolar absolute differential confocal approach to higher spatial resolution," Opt. Express **12**(21), 5013–5021 (2004).
17. W. Zhao, C. Liu, and L. Qiu, "Laser divided-aperture differential confocal sensing technology with improved axial resolution," Opt. Express **20**(23), 25979–25989 (2012).
18. S. Kimura and T. Wilson, "Effect of axial pinhole displacement in confocal microscopes," Appl. Opt. **32**(13), 2257–2261 (1993).
19. G. S. Kino and T. R. Corle, *Confocal Scanning Optical Microscopy and Related Imaging Systems* (Academic, 1996).

1. Introduction

Confocal microscopy (CM) has unique optical section capability and superior lateral resolution, and can be easily fitted with a pupil filter to achieve optical super resolution [1–7]. Thus, CM has an important function in both fundamental academic research and industrial applications, such as microelectronics, industrial precision detection, biomedicine and materials engineering [8–12]. However, the existing CM imaging method has the following deficiencies: (a) low imaging efficiency because of layer-by-layer scanning by the focus, (b) low axial depth resolution because of the detection focus corresponding to the axial response curve's peak with the lowest sensitivity, and (c) low signal-to-noise ratio (SNR) because of ambient lighting and the power disturbance of the light source.

Lee et al. proposed a differential confocal microscopy (DCM) using the sharp slopes of the CM axial curve [13]. DCM achieved the high-speed imaging of homogeneous samples by single-layer scanning with depth resolution of up to 2 nm. By scanning the sample twice with a fixed vertical offset, DCM separated the signal that comes from surface heterogeneity from the topographic signal and obtained 10-nm depth resolution for samples with reflectivity heterogeneity [14]. However, DCM works in the defocus linear segment of the CM axial response curve, which leads to decreases in lateral resolution [15]. Besides, DCM is susceptible to power disturbances of the light source, ambient lighting and the reflection characteristics of the sample surface.

To solve the aforementioned problems, we proposed a bipolar absolute differential confocal microscopy (BADCM) [16, 17]. The BADCM divides the confocal microscopy detection light path into two detection paths before and after focus, and the detectors of the two detection paths have an equal axial offset oriented in opposite direction from the focal plane of the collecting lens. By the subtraction of the two signals simultaneously detected from the two detection paths, BADCM yielded a new differential confocal imaging characteristic curve. BADCM features better sensor linearity, higher axial resolution, and better SNRs than DCM. Most importantly, BADCM has a bipolar measurement range and an absolute zero, which facilitates the expansion of the measurement range. Unfortunately, the BADCM axial response is also affected by the sample reflectivity, and thus it cannot be used in the profile imaging for the samples with surface heterogeneity. Besides, BADCM has a declining lateral resolution due to the larger detector axial offset.

To realize the rapid imaging for samples with reflectivity heterogeneity and address the deficiencies described above, a real-time laser differential confocal microscopy (RLDCM) without sample reflectivity difference effects is proposed based on the same optical path arrangement as BADCM. A RLDCM system is successfully developed to achieve real-time three-dimension (3-D) imaging of height topography of sample surface. By dividing the difference of the two signals simultaneously detected from two confocal imaging paths before and after focus by the higher signal between these two signals, the RLDCM separates the signal that comes from reflectivity heterogeneity from the topographic signal in real time for the first time. By optimizing the axial detector offset, RLDCM improves the axial resolution without reducing lateral resolution in comparison with DCM and BADCM. In addition, RLDCM has excellent suppression capability of noise and disturbance.

2. RLDCM imaging principle

As shown in Fig. 1, RLDCM divides the confocal microscopy light path into confocal imaging path A after the focus in the dash-dotted area and confocal imaging path B before the

#214706 - $15.00 USD Received 25 Jun 2014; revised 13 Aug 2014; accepted 24 Aug 2014; published 29 Aug 2014

focus in the dashed area. By dividing the differential signal of the two signals simultaneously detected from the two confocal imaging paths A and B by the higher signal between these two signals, RLDCM yields a normalized axial response curve to directly achieve the surface profile imaging.

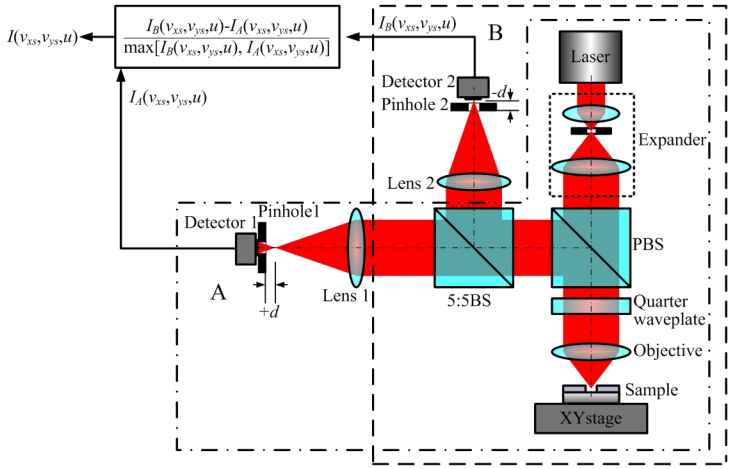

Fig. 1. Schematic diagram of RLDCM.

RLDCM imaging process is described as follows: the light coming from a laser passes through an expander and a polarization beam splitter (PBS), and *p*-polarized light transmitted is used as the measurement light. The measurement light passes through a quarter-wave plate and is focused onto the sample surface by the objective, and the light that is reflected from the sample passes through the quarter-wave plate again and is converted into *s*-polarized light. The *s*-light is divided by a 5:5 beam splitter (BS) into two components, and they are focused by collecting lenses 1 and 2 and detected by detectors 1 and 2 placed close to pinholes 1 and 2,respectively. Pinhole 1 is placed after the focal plane of lens 1, and the distance between the focal plane and pinhole 1 is d; pinhole 2 is placed before the focal plane of lens 2, and the distance between the focal plane and pinhole 2 is also d. The optical normalized coordinate corresponding to distance d is expressed as u_d. The PBS and the quarter-wave plate can make the light reflected from the sample fully enter into the detection paths and not give back to laser source.

When the sample is scanned to a position (v_{xs},v_{ys}), the signal received by detector 1 in imaging path A is $I_A(v_{xs},v_{ys},u)$, and the signal received by detector 2 in imaging path B is $I_B(v_{xs},v_{ys},u)$. According to confocal imaging formula [1], the signals are

$$\begin{aligned} I_A(v_{xs},v_{ys},u) &= \left|\left[R(v_{xs},v_{ys})h_1(v_{xs},v_{ys},u)h_{A2}(v_{xs},v_{ys},u,+u_d)\right]\otimes_3 o(v_{xs},v_{ys},u)\right|^2, \\ I_B(v_{xs},v_{ys},u) &= \left|\left[R(v_{xs},v_{ys})h_1(v_{xs},v_{ys},u)h_{B2}(v_{xs},v_{ys},u,-u_d)\right]\otimes_3 o(v_{xs},v_{ys},u)\right|^2. \end{aligned} \quad (1)$$

where $\otimes_3$ denotes the 3-D convolution operation; $h_1(v_{xs},v_{ys},u)$ is 3-D amplitude point spread function (APSF) for the point source; $h_{A2}(v_{xs},v_{ys},u,u_d)$ and $h_{B2}(v_{xs},v_{ys},u,-u_d)$ are the 3-D APSF for the point detectors of imaging paths A and B, respectively [1]; $o(v_{xs},v_{ys},u)$ is the 3-D amplitude object function of the sample; u is the axial optical normalized coordinate and denotes the sample height relative to the objective focal plane in agreement with the reference plane of the sample; and $R(v_{xs},v_{ys})$ is the amplitude reflectivity function of the sample. v_{xs} and v_{ys} are the lateral optical normalized coordinates.

The differential signal $I_d(v_{xs},v_{ys},u)$ and the higher signal $I_{max}(v_{xs},v_{ys},u)$ of these two signals are

#214706 - $15.00 USD Received 25 Jun 2014; revised 13 Aug 2014; accepted 24 Aug 2014; published 29 Aug 2014

$$
\begin{aligned}
I_d(v_{xs},v_{ys},u) &= I_B(v_{xs},v_{ys},u) - I_A(v_{xs},v_{ys},u),\\
I_{\max}(v_{xs},v_{ys},u) &= \max[I_A(v_{xs},v_{ys},u), I_B(v_{xs},v_{ys},u)]\\
&= \begin{cases} I_B(v_{xs},v_{ys},u), I_B(v_{xs},v_{ys},u) \ge I_A(v_{xs},v_{ys},u) \\ I_A(v_{xs},v_{ys},u), I_B(v_{xs},v_{ys},u) < I_A(v_{xs},v_{ys},u) \end{cases}.
\end{aligned} \tag{2}
$$

By dividing $I_d(v_{xs},v_{ys},u)$ by $I_{\max}(v_{xs},v_{ys},u)$, the height profile signal $I(v_{xs},v_{ys},u)$ obtained is

$$
I(v_{xs},v_{ys},u) = \frac{I_d(v_{xs},v_{ys},u)}{I_{\max}(v_{xs},v_{ys},u)} = \begin{cases} 1 - \dfrac{I_A(v_{xs},v_{ys},u)}{I_B(v_{xs},v_{ys},u)}, I_B(v_{xs},v_{ys},u) \ge I_A(v_{xs},v_{ys},u) \\ \dfrac{I_B(v_{xs},v_{ys},u)}{I_A(v_{xs},v_{ys},u)} - 1, I_B(v_{xs},v_{ys},u) < I_A(v_{xs},v_{ys},u) \end{cases} \tag{3}
$$

Substituting Eq. (1) into Eq. (3) and assuming that the amplitude reflectivity $R(v_{xs},v_{ys})$ within the light spot is a constant R, then the height signal $I(v_{xs},v_{ys},u)$ for $I_B(v_{xs},v_{ys},u) \ge I_A(v_{xs},v_{ys},u)$ is

$$
\begin{aligned}
I(v_{xs},v_{ys},u) &= 1 - \frac{\left| \left[R h_1(v_{xs},v_{ys},u) h_{\mathrm{A2}}(v_{xs},v_{ys},u,+u_d) \right] \otimes_3 o(v_{xs},v_{ys},u) \right|^2}{\left| \left[R h_1(v_{xs},v_{ys},u) h_{\mathrm{B2}}(v_{xs},v_{ys},u,-u_d) \right] \otimes_3 o(v_{xs},v_{ys},u) \right|^2}\\
&= 1 - \left| \frac{\left[h_1(v_{xs},v_{ys},u) h_{\mathrm{A2}}(v_{xs},v_{ys},u,+u_d) \right] \otimes_3 o(v_{xs},v_{ys},u)}{\left[h_1(v_{xs},v_{ys},u) h_{\mathrm{B2}}(v_{xs},v_{ys},u,-u_d) \right] \otimes_3 o(v_{xs},v_{ys},u)} \right|^2.
\end{aligned} \tag{4}
$$

It can be seen from Eq. (4) that the reflectivity factor R is eliminated, and the height profile signal $I(v_{xs},v_{ys},u)$ in RLDCM is only dependent on u_d and u and is invariable with the sample reflectivity R.

In similarly, the result about signal $I(v_{xs},v_{ys},u)$ still exists for $I_B(v_{xs},v_{ys},u) < I_A(v_{xs},v_{ys},u)$.

The axial response formula of confocal microscope with axial detector offset is [18];

$$
I(u,u_d) = \left\{ \frac{\sin[(2u+u_d)/4]}{(2u+u_d)/4} \right\}^2 = \mathrm{sinc}^2\left(u/2 + u_d/4\right) \tag{5}
$$

When a flat mirror of amplitude reflectivity R is scanned in the axial direction by RLDCM, the confocal axial responses of imaging paths A and B are

$$
I_A(u,u_d) = R^2 \,\mathrm{sinc}^2\left(u/2 + u_d/4\right), I_B(u,-u_d) = R^2 \,\mathrm{sinc}^2\left(u/2 - u_d/4\right) \tag{6}
$$

Substituting Eq. (6) into Eq. (3), the RLDCM axial response formula is

$$
I(u,u_d) = \begin{cases} 1 - \mathrm{sinc}^2\left(u/2 + u_d/4\right) \Big/ \mathrm{sinc}^2\left(u/2 - u_d/4\right), I_B(u,u_d) \ge I_A(u,u_d) \\ \mathrm{sinc}^2\left(u/2 - u_d/4\right) \Big/ \mathrm{sinc}^2\left(u/2 + u_d/4\right) - 1, I_B(u,u_d) < I_A(u,u_d) \end{cases}. \tag{7}
$$

It can be seen from Eq. (7) that RLDCM's axial response is nothing to the sample reflectivity R^2, and the theoretical output range of $I(u,u_d)$ is [-1,1]. The RLDCM axial response curves achieved by using Eq. (7) are shown in Fig. 2.

#214706 - $15.00 USD Received 25 Jun 2014; revised 13 Aug 2014; accepted 24 Aug 2014; published 29 Aug 2014

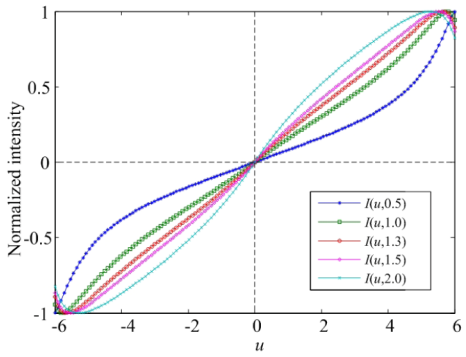

Fig. 2. RLDCM axial response curvess at various u_d.

When u_d changes from 0.5 to 2.0, the slope of the RLDCM axial curve $I(u,u_d)$ increases with increasing u_d, while the linear range of $I(u,u_d)$ initially increases and then decreases (Fig. 2).

For a given u_d, $I(u,u_d)$ is a monotonic function of u in a certain range. Therefore,

$$u(v_{xs}, v_{ys}) = f\left[I(v_{xs}, v_{ys}) \right]. \tag{8}$$

where $f(\cdot)$ is the sensing function determined by the curve fitting of axial response curve with given u_d.

During the scanning, $I_A(v_{xs},v_{ys},u)$ and $I_B(v_{xs},v_{ys},u)$ are detected simultaneously and $I(v_{xs},v_{ys},u)$ can be calculated by Eq. (3) instantly, so RLDCM can separate the signal that comes from reflectivity heterogeneity from the topographic signal in real time. Therefore, measurements for samples with or without reflectivity heterogeneity can be performed at high speed by single-layer scanning. In comparison with CM and DCM, RLDCM imaging time is dramatically smaller than CM imaging time, while RLDCM imaging time is half of DCM imaging time for samples with reflectivity heterogeneity and is the same as DCM imaging time for samples without reflectivity heterogeneity.

In a word, RLDCM realizes a new microscopy technology for imaging height topography of sample surface and is capable of imaging samples with or without reflectivity heterogeneity in real time at high speed.

3. Imaging characteristic analysis and simulation

The RLDCM advantages are verified by the theoretical analysis and simulation. The optimization of offset u_d, the elimination of reflectivity effect, axial and lateral responses and noise suppression are simulated and discussed in theory. Theoretical analysis and simulation results demonstrate that RLDCM is able to accurately distinguish between the signal drop from height drop and the signal drop from reflectivity drop; and RLDCM has a higher axial resolution and an improved lateral resolution compared with DCM and BADCM and has excellent suppression capability of noise and disturbance. According to the simulation results, the RLDCM's height imaging range is limited to $u \in [-2.8, +2.8]$.

3.1 Optimization for axial detector offset u_d and axial response analysis

As shown in Fig. 2, the linearity and sensitivity of the RLDCM's axial response are determined by axial detector offset u_d. When $u_d = 1.3$, the RLDCM's axial curve has the best fitting line and the longest linear range of $u \in [-5.5, 5.5]$.

For $u \in [-5.5, 5.5]$, curve $I(u,u_d)$ are fitted to determine the most feasible u_d. The coefficient of determination R-squared and axial resolution $\Delta E/r$ of the fitting curve for different u_d are shown in Fig. 3. Here, ΔE is the root-mean-square fitting error and r is the slope of the fitting curve. When $u_d = 1.27$ (Fig. 3), the maximum R-squared and the minimum

#214706 - $15.00 USD Received 25 Jun 2014; revised 13 Aug 2014; accepted 24 Aug 2014; published 29 Aug 2014

$\Delta E/r$ are obtained and the axial response curve has the best linearity. And The RLDCM's axial response curve $I(u,1.27)$ and the fitting curve $I_F(u,1.27)$ are shown in Fig. 4.

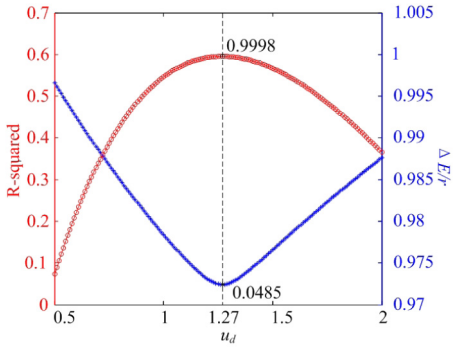

Fig. 3. R-squared and $\Delta E/r$ curves with different u_d.

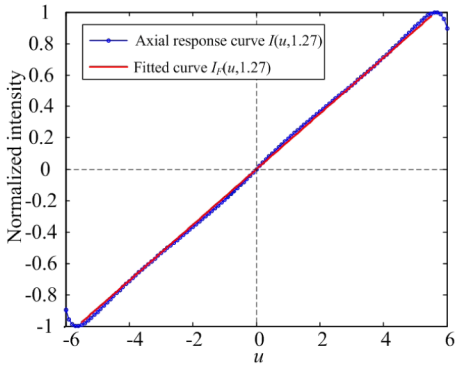

Fig. 4. RLDCM's axial response curve with u_d = 1.27.

As shown in Fig. 4, the signal intensity of the RLDCM's axial response curve $I(u,1.27)$ is proportional to the defocus distance u between the surface under test and the objective focal plane, RLDCM can realize the imaging of surface profiles using this axial response curve. The slope of the fitted curve $I_F(u,1.27)$ is 0.1803, thus the theoretical axial resolution of RLDCM is $\Delta E/0.1803$ in optical coordinates or $0.22\Delta E\lambda/\sin^2(a_0/2)$ in physical coordinates. Here, a_0 is half of objective aperture angle. Obviously, a larger $\sin a_0$ results in the better axial resolution. When $\sin a_0$ is confirmed, improving the RLDCM's noise suppression ability to reduce ΔE can improve the axial resolution. Analysis of these axial response characteristics indicates that the RLDCM can realize high axial resolution imaging of the surface profiles by an optimized offset u_d = 1.27 for samples with reflectivity heterogeneity .

3.2 Reflectivity elimination effect

The reflectivity elimination effect is verified by the height-step imaging. The height and the amplitude reflectivity of the step are

$$u(v_x)=\begin{cases}u_t, v_x \ge 0\\ u_b, v_x < 0\end{cases}, R(v_x)=\begin{cases}R_t, v_x \ge 0\\ R_b, v_x < 0\end{cases} \tag{9}$$

where u_t and u_b are the height at the top and bottom of the step, respectively, and R_t and R_b are the amplitude reflectivity at the top and bottom of the step, respectively. The objective is focused at u = 0, the step imaging with height or reflectivity change obtained by using Eqs.

#214706 - $15.00 USD Received 25 Jun 2014; revised 13 Aug 2014; accepted 24 Aug 2014; published 29 Aug 2014

(1)–(3) and Eq. (8) are shown in Fig. 5, Fig. 6, Fig. 7, and Fig. 8, in which curve I_C is the confocal imaging curve with $u_d = 0$.

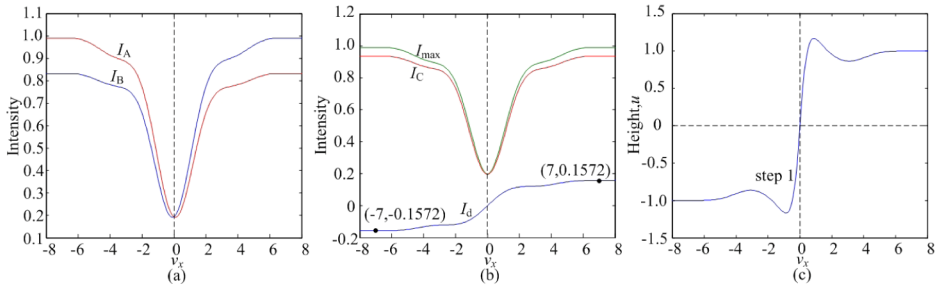

Fig. 5. Simulation RLDCM imaging curves of height-step 1 with $u_t = 1$, $u_b = -1$, $R_t = 1$ and $R_b = 1$. (a) I_A and I_B curves. (b) I_C, I_{max} and I_d curves. (c) Height curve.

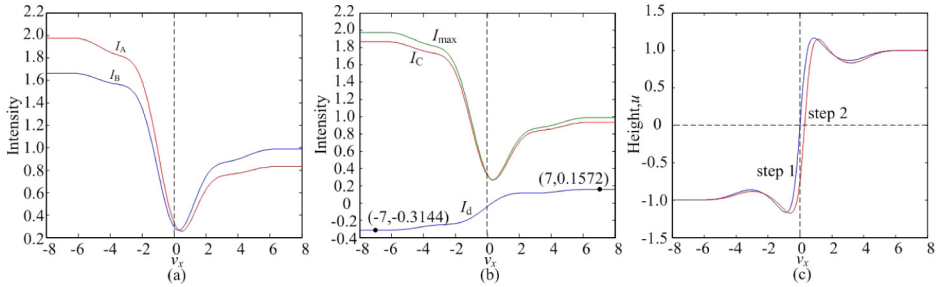

Fig. 6. Simulation RLDCM imaging curves of height-step 2 with $u_t = 1$, $u_b = -1$, $R_t = 1$ and $R_b = 2^{1/2}$. (a) I_A and I_B curves. (b) I_C, I_{max} and I_d curves. (c) Height curves.

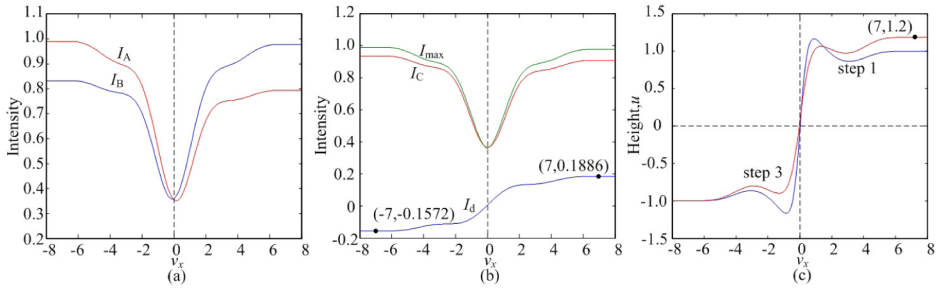

Fig. 7. Simulation RLDCM imaging curves of height-step 3 with $u_t = 1.2$, $u_b = -1$, $R_t = 1$ and $R_b = 1$. (a) I_A and I_B curves. (b) I_C, I_{max} and I_d curves. (c) Height curves.

#214706 - $15.00 USD Received 25 Jun 2014; revised 13 Aug 2014; accepted 24 Aug 2014; published 29 Aug 2014

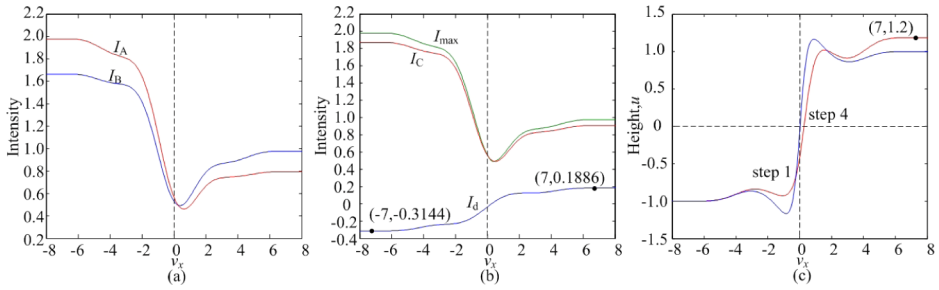

Fig. 8. Simulation RLDCM imaging curves of height-step 4 with $u_t = 1.2$, $u_b = -1$, $R_t = 1$and $R_b = 2^{1/2}$. (a) I_A and I_B curves. (b) I_C, I_{max} and I_d curves. (c) Height curves.

Figures 5–8 show that both height changes and the reflectivity changes can make curves I_A and I_B change in the intensity and further make curves I_{max} and I_d change in intensity. The intensity profile I_{max} is quite similar to the intensity profile I_C in shape, and it shows the reflectivity of the step. Curve I_d shows the height of the step, and height u deviates at the edge location caused by the reflectivity change [Figs. 6(c) and 8(c)].

The ability of distinguishing signal change caused by height change or reflectivity change is determined by I_d and u values at $v_x = -7$ and $v_x = 7$ (shown in Table 1).

Table 1. Comparison of Height-Steps Imaging

	Features	I_d	u
Step 1	u_t=1, u_b=-1, R_t=1, R_b=1	$I_d(7)$=0.1572, $I_d(-7)$=-0.1572	$u(7)$=1, $u(-7)$=-1
Step 2	u_t=1, u_b=-1, R_t=1, $\boldsymbol{R_b=2^{1/2}}$	$I_d(7)$=0.1572, $\boldsymbol{I_d(-7)=-0.3144}$	$u(7)$=1, $\boldsymbol{u(-7)=-1}$
Step 3	$\boldsymbol{u_t=1.2}$, u_b=-1, R_t=1, R_b=1	$\boldsymbol{I_d(7)=0.1886}$, $I_d(-7)$=-0.1572	$\boldsymbol{u(7)=1.2}$, $u(-7)$=-1
Step 4	$\boldsymbol{u_t=1.2}$, u_b=-1, R_t=1, $\boldsymbol{R_b=2^{1/2}}$	$\boldsymbol{I_d(7)=0.1886}$, $\boldsymbol{I_d(-7)=-0.3144}$	$\boldsymbol{u(7)=1.2}$, $\boldsymbol{u(-7)=-1}$

The comparisons shown in Table 1 indicate that the change only from the height of the sample causes the change of signal u, and the change from the reflectivity of the sample has no influence on signal u at the area far from the step edge, and therefore, RLDCM successfully separates the signal changes that come from reflectivity for the sample with both height and reflectivity changes,

The height-step imaging results demonstrate that RLDCM features a good reflectivity elimination effect and is able to accurately distinguish the signal drop from height drop and the signal drop from reflectivity drop.

3.3 Lateral response analysis

The RLDCM's lateral response is verified by RLDCM imaging of height-step with homogeneous reflectivity. Here $u_t = 1$, $u_b = -1$, $R_t = 1$ and $R_b = 1$. When the objective is focused at $u = 0$, the imaging of height-step with homogeneous reflectivity obtained by using CM, DCM and BADCM are shown in Fig. 9.

#214706 - $15.00 USD Received 25 Jun 2014; revised 13 Aug 2014; accepted 24 Aug 2014; published 29 Aug 2014

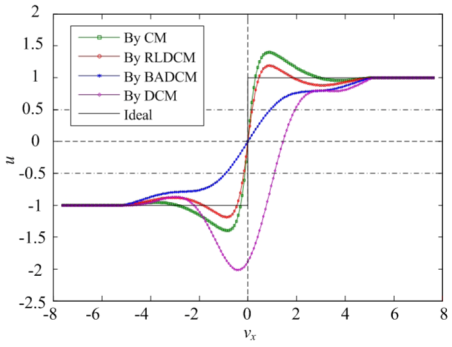

Fig. 9. Simulation of the imaging curves of the height-step using CM, RLDCM, BADCM and DCM.

As shown in Fig. 9, RLDCM obtains the height profile similar to the best height profile obtained by CM, and the edge overshoot of RLDCM image is smaller than that of CM image. DCM suffers a strong overshoot at the edge and is not suitable for surface precision measurement. BADCM suffers the serious lateral resolution reduction and is not suitable for high-resolution surface imaging. Edge rise distance (ERD) and edge slope (ES) are used to characterize the imaging lateral resolution (Table 2). ERD is the physical interval in which the height u increases from −0.5 to 0.5. ES is the slope of curve corresponding to ERD. Table 2 shows that CM has the best lateral responses with the largest ES and the narrowest ERD and RLDCM has the improved ERD and ES close to CM, while BADCM has the worst lateral responses with the smallest ES and the widest ERD. Compared with BADCM and DCM, RLDCM significantly improves the lateral resolution and suppresses the overshoot at the edge.

Table 2. Comparison of ERDs and ESs

Method	ERD		ES	
	Value	Deviation from CM	Value	Deviation from CM
CM	0.254	–	3.937	–
RLDCM	0.349	37%	2.865	−27%
DCM	0.849	234%	1.178	−70%
BADCM	1.752	580%	0.571	−85%

3.4 Influence of surface structure defocusing on the lateral response

The surface structure defocusing influences the RLDCM's lateral response during surface profile imaging and the lateral resolution of optical intensity images of I_A and I_B. The defocusing intensity point spread function (IPSF) of the confocal imaging path A is [1]

$$\left|h_A(v,u,+1.27)\right|^2=\left|\int_0^1 P(\rho)\exp(\frac{iu\rho^2}{2})J_0(v\rho)\rho d\rho\int_0^1 P(\rho)\exp[\frac{i(u+1.27)\rho^2}{2}]J_0(v\rho)\rho d\rho\right|^2, \tag{10}$$

where $P(\rho)$ is the lens pupil function, ρ is a radial normalized radius; J_0 is a zero-order Bessel function; u and v are axial and lateral optical normalized coordinates, respectively. The curves $|h_A(v,u+1.27)|^2$ with different defocusing distances u are shown in Fig. 10.

#214706 - $15.00 USD Received 25 Jun 2014; revised 13 Aug 2014; accepted 24 Aug 2014; published 29 Aug 2014

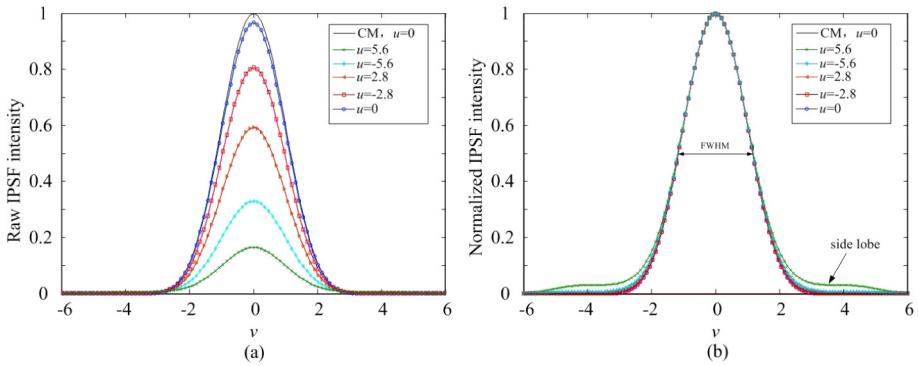

Fig. 10. Defocusing IPSF curves |hA(v,u + 1.27)|2 of confocal imaging path A. (a) Raw curves, and (b) Normalized curves.

With increasing $|u + 1.27|$, IPSF curve's top value decreases gradually [Fig. 10(a)], while IPSF curve's full width at half maximum decreases slightly and the side lobe increases gradually [Fig. 10(b)]. The decrease in top value causes the image intensity to reduce, while the increase in side lobe causes the image quality of I_A and I_B to decrease. Both cases will decrease surface profile imaging quality.

The simulation imaging curves of a height-step with u_t-u_b = 2, R_t = 1 and R_b = 1 are used to investigate the influence of surface structure defocusing on the lateral response (Fig. 11). u_t changes from 1 to 5.6 and u_b = u_t-2. The objective is focused at u = 0. The height-step defocusing relative to the focal plane is equal to u_t.

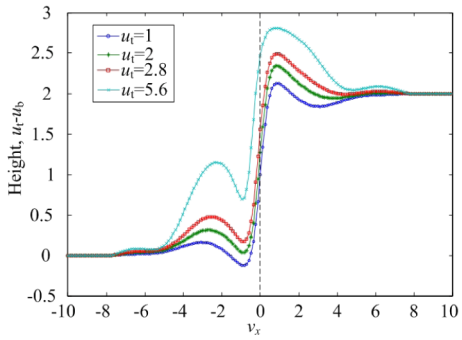

Fig. 11. The profile image curves with different u_t.

With increasing u_t, the edge overshoot of the height profile image curve increases seriously, and the height profile imaging quality worsens (Fig. 11). When u_t = 1, the objective is focused at the middle of the step and the imaging curve is the best. When u_t = 2.8, the height profile image curve is still available compared with the image curve of u_t = 1. When u_t = 5.6, the height profile image curve shows serious edge overshoot.

To ensure larger optical imaging intensity and better height profile imaging quality, the RLDCM's height imaging range must be limited to $u \in [-2.8, +2.8]$. In this case, RLDCM has lateral response similar to CM.

3.5 Noise suppression analysis

CM suffers from the multiplicative and additive noises. Multiplicative noise is mainly caused by power disturbances of the light source. Additive noise is mainly caused by ambient light and photoelectric detector circuit noises. The proportion of multiplicative noise to the ideal signal is noted as η, which satisfies $1 + \eta \approx 1$. The circuit noises of imaging paths A and B are n_A and n_B, respectively. Hence, $I'_A = (1 + \eta) I_A + n_A$, $I'_B = (1 + \eta) I_B + n_B$ and $\Delta n = n_B - n_A \approx 0$.

#214706 - $15.00 USD Received 25 Jun 2014; revised 13 Aug 2014; accepted 24 Aug 2014; published 29 Aug 2014

If the system only suffers from multiplicative noise, the influence of multiplicative noise can be completely eliminated [Eq. (4)]. The ideal signal calculated from I_A and I_B is denoted as I and the signal calculated from I'_A and I'_B is denoted as I'. Considering these noises at the same time, in the case of $I_A' > I_B'$, $|n_B/I'_B| > |n_A/I'_A| \approx 0$, and

$$\left|I' - I\right| = \left|\left\{\frac{[(1+\eta)I_B + n_B]}{(1+\eta)I_A + n_A} - 1\right\} - \left[\frac{I_B}{I_A} - 1\right]\right| = \left|\frac{\Delta n - In_A}{I_A + \eta I_A + n_A}\right| \approx \left|I\frac{n_A}{I'_A}\right|. \qquad (11)$$

The influence of additive noise n_A is further reduced by I and I'_A [Eq. (11)]. When u_d = 1.27, the RLDCM's imaging range is $|I| \le 0.5$, thus RLDCM shows excellent suppression capability of noise and disturbance, which improves the axial resolution of the system.

4. Imaging experiment

A RLDCM system shown in Fig. 12 is constructed. A long-travel high-speed piezo-driven microscope objective nanofocusing/scanning z-driver with direct metrology P725.4 CD (Physik Instrumente, Germany) is used to drive the objective. PI P725.4 is equipped with absolute-measuring direct-metrology capacitive sensors and can scan and position objectives with sub-nanometer resolution. A fast and highly accurate multi-axis scanning and nanopositioning stage of PI P563 (Physik Instrumente) with flatness and straightness in the nanometer range is used to realize the sample scanning in the x-y direction. The laser wavelength is 632.8 nm and the sine of half-aperture angle of the objective is 0.80.

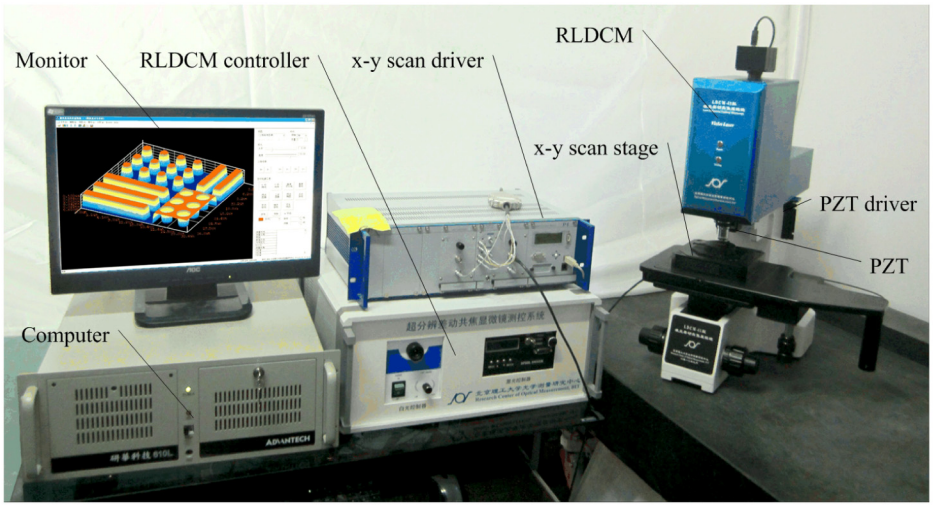

Fig. 12. Real-time laser differential confocal microscope.

4.1 RLDCM axial response test

The measured axial response curve is shown in Fig. 13(a), and fitting height sensing curve is shown in Fig. 13(b). The difference between the measured and theoretical curves is caused by finite size effects of the detector and optical system aberrations. The height imaging range of the measured axial response is 0.6567 μm, and the output surface profile signal is ± 0.4 V. To improve the measurement accuracy, the cubic polynomial fitting is used to fit the height sensing curve. From the obtained fitting equation, the axial response sensitivity is 0.6874 V/μm and the measured axial resolution is 2.2 nm. So, RLDCM has the axial resolution better than DCM with axial resolution of 10nm [14] and similar to BADCM [16].

#214706 - $15.00 USD Received 25 Jun 2014; revised 13 Aug 2014; accepted 24 Aug 2014; published 29 Aug 2014

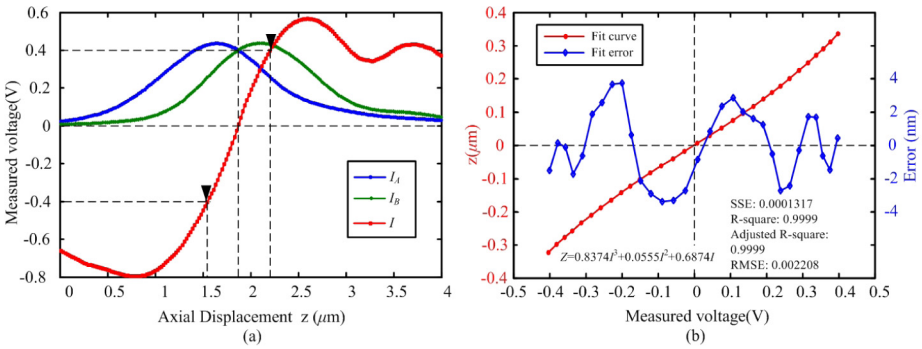

Fig. 13. Measured axial response curve and fitted height sensing curve. (a) Measured axial response curve; and (b) Fitted height sensing curve.

4.2 Imaging experiment of height standard

A RLDCM 3-D imaging is realized for the first time to verify the reflectivity elimination effect and the surface measurement accuracy. The line structures of HS-500MG are scanned. The HS-500MG height standard introduced by BudgetSensors features Silicon Dioxide structure arrays on a 5 × 5 mm Silicon chip. The fabrication process guarantees excellent uniformity of the structures across the chip. The Silicon Dioxide structure has a step height of 500nm and a pitch of 5 μm [Fig. 14(a)]. The CM images obtained by Olympus LEXT 4000 indicate that the Silicon Dioxide structure [dark part in Fig. 14(b), red part in Fig. 14(c)] has the reflectivity lower than the Silicon base [bright part in Fig. 14(b), blue part in Fig. 14(c)]. The height and period, and edge width of the step are measured precisely by DI Dimension 3100 Atomic Force Microscopy (AFM) [Fig. 14(d)].

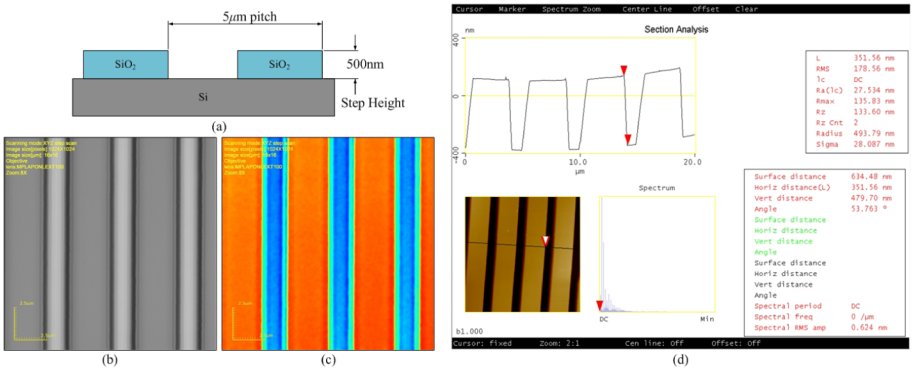

Fig. 14. The line structures of HS–500MG. (a) the cross-section view of the structures.(b) Full-focus intensity image of the structures obtained by CM. (d) Height image of the structures obtained by CM. (d) Height measurements of the structures scanned by AFM.

The measurements of the line structures obtained by RLDCM are shown in Fig. 15. The image size is 256 × 256 pixels and the imaging range is 18.73 μm × 18.73 μm. The I_{max} image and the height image are calculated by images I_A and I_B simultaneously from the scan and the intensity difference between I_A and I_B images is caused only by the variation of the sample height. I_{max} image shown in Fig. 15(c) is similar to the Full-focus intensity image obtained by CM shown in Fig. 14(b), and shows the variation of the sample in the reflectivity. Height image z_m obtained by RLDCM shown in Fig. 15(d) is similar to the height image obtained by CM shown Fig. 14(c), and shows the variation of the sample in the height.

#214706 - $15.00 USD Received 25 Jun 2014; revised 13 Aug 2014; accepted 24 Aug 2014; published 29 Aug 2014

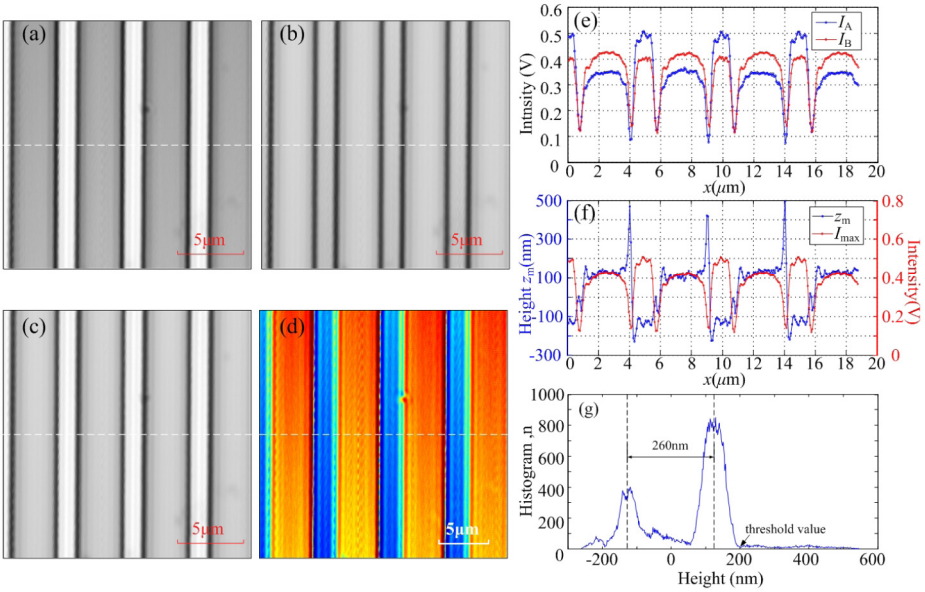

Fig. 15. The measurements of the line structures scanned by RLDCM. (a) I_A image. (b) I_B image. (c) I_{max} image. (d) Height image z_m. (e) I_A and I_B intensity profile at the position indicated by the dashed lines in (a) and (c). (f) I_{max} intensity profile and z_m height profile at the position indicated by the dashed lines in (c) and (d). (g) Histogram for z_m.

The measurements demonstrate that RLDCM successfully eliminates the effect of the reflectivity variation and obtains the surface profile of the line structures in real-time.

As shown in Fig. 15(f), there are sharp spikes on the upper right region of each step. These sharp spikes are caused by complex diffraction at the sharp edges. The intensities at the spikes in intensity curve I_{max} are very weak so that these spikes are of low credibility. A threshold value of 0.2μm for spikes is obtained by the histogram analysis of height image z_m shown in Fig. 15 (g). The measured height data of spikes can be express as $z_m' = \{z_m | z_m \geq 0.2\mu m\}$. Let $z_m' = 0.2\mu m$ at these spikes, then the spikes are eliminated.

The measured height shown in Fig. 15 (f) is not in well agreement with that shown in Fig. 14(d) measured by AFM. This is because the light received from the Silicon Dioxide structure area is reflected in fact from the Silicon base below the Silicon Dioxide structure. According to the previous research, the true height profile can be obtained by [19]:

$$\frac{h}{h_m} = \frac{\int_0^{\alpha_0} \frac{\sqrt{n^2 - \sin^2\theta}}{\cos\theta} \sin\theta d\theta}{\int_0^{\alpha_0} \sin\theta d\theta}, \tag{12}$$

where h_m is the measured step height, h is the true step height; n = 1.5517 is the silica refractive index, and sine of half the aperture angle of the objective is sin a_0 = 0.80. Thus, h/h_m = 1.8196 and the true height data are calculated.

After the high frequency noise in the true height data is eliminated by two-dimension low-pass filter, the 3-D surface profile is shown in Fig. 16.

#214706 - $15.00 USD Received 25 Jun 2014; revised 13 Aug 2014; accepted 24 Aug 2014; published 29 Aug 2014

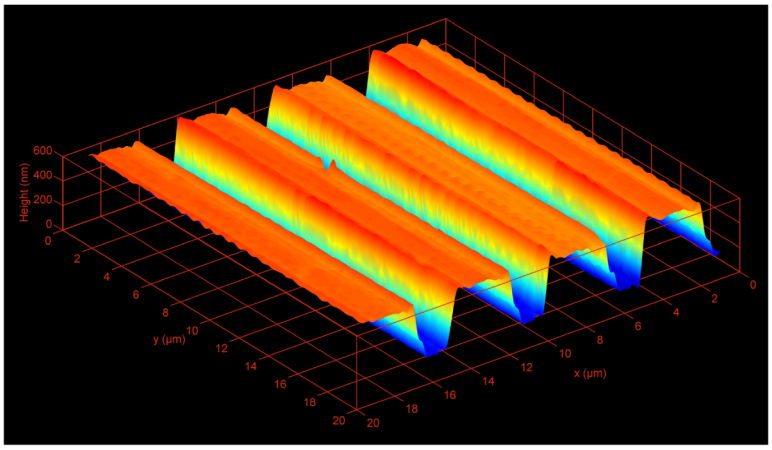

Fig. 16. 3-D surface profile of HS-500MG obtained by RLDCM.

To achieve the precision measurement of step edge width, step height and step period, the least square planar fitting is used for the filtered height to get the estimation height data, which determines the edge location precisely. As shown in Fig. 17, the estimation curve is benefit for the edge positioning more than filtered curve and the measurements from Fig. 17 is shown in Table 3.

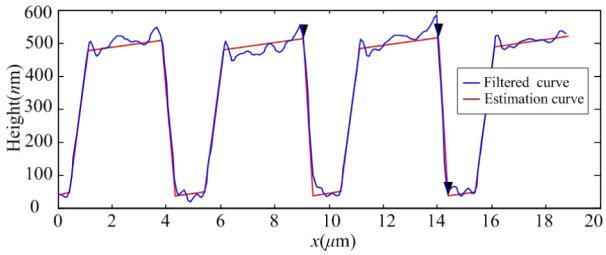

Fig. 17. Filtered and estimation curves of true height profile at the position indicated by the dashed line in Fig. 15(d).

Table 3. Measurement Comparison between RLDCM and AFM

	Step edge width (μm)	Step period (μm)	Step height (nm)
RLDCM	0.361	4.988	478
AFM	0.3516	5.0054	479.70
Deviation	0.0094	−0.0174	−1.70

As shown in Table 3, the measurements obtained by RLDCM are in well agreement with that obtained by AFM and demonstrate the good 3-D imaging and measurement performance of RLDCM.

Experimental results show that RLDCM eliminates the line structures' reflectivity heterogeneity during height profile imaging and achieves the accurate imaging and measurement. In addition, RLDCM can also be applicable to semiconductor metrology, MEMS inspection and line-width measurement.

#214706 - $15.00 USD Received 25 Jun 2014; revised 13 Aug 2014; accepted 24 Aug 2014; published 29 Aug 2014

5 Conclusions

A new RLDCM without sample reflectivity difference effects is proposed for rapid high-resolution single-layer scanning and high SRN surface imaging. The proposed RLDCM realizes the height topography imaging by dividing the difference between the two signals simultaneously detected from two confocal imaging paths before and after focus by the higher signal between these two signals, and it separates the signal that comes from reflectivity heterogeneity from the topographic signal in real time for the first time. Based on the proposed RLDCM, a RLDCM system is successfully fabricated for 3-D imaging of a sample surface profile. Theoretical analysis and experiments demonstrate that RLDCM significantly reduces the height topography imaging time by single-layer scanning for the sample surface with reflectivity heterogeneity and achieves the high axial resolution of 2 nm without losing lateral resolution by optimizing the axial detector offset. And RLDCM has excellent suppression capability of noise and disturbance. In addition, RLDCM is applicable to semiconductor metrology, MEMS inspection, device fabrication monitoring in situ, and observation of morphology changes or cellular membrane motion of live biological samples.

Acknowledgment

The authors gratefully acknowledge support from the National Science Foundation of China (No.91123014), the National High Technology Research and Development Program of China (No.SS2012AA040507), and National Instrumentation Program (NIP, No.2011YQ04013601).

#214706 - $15.00 USD Received 25 Jun 2014; revised 13 Aug 2014; accepted 24 Aug 2014; published 29 Aug 2014